Acta Crystallographica Section B
Structural Science
ISSN 0108-7681

Structures of 6*H* perovskites $Ba_3CaSb_2O_9$ and $Ba_3SrSb_2O_9$ determined by synchrotron X-ray diffraction, neutron powder diffraction and *ab initio* calculations

Budwy Rowda,[a] Maxim Avdeev,[b] Peter L. Lee,[c] Paul F. Henry[d] and Chris D. Ling[a,b]*

[a]School of Chemistry, The University of Sydney, Sydney 2006, Australia, [b]Bragg Institute, ANSTO, PMB 1, Menai 2234, Australia, [c]Advanced Photon Source, Argonne National Laboratory, Argonne, IL 60439, USA, and [d]Institut Laue–Langevin, 6 rue Jules Horowitz, 38042 Grenoble CEDEX 9, France

Correspondence e-mail: c.ling@chem.usyd.edu.au

Received 8 November 2007
Accepted 22 February 2008

The structures of the 6*H* perovskites $Ba_3B^{2+}Sb^{5+}{}_2O_9$, *B* = Ca and Sr, have been solved and refined using synchrotron X-ray and neutron powder diffraction data. $Ba_3CaSb_2O_9$ and $Ba_3SrSb_2O_9$ have monoclinic $C2/c$ and triclinic $P\bar{1}$ space-group symmetries, respectively, while $Ba_3MgSb_2O_9$ has ideal hexagonal $P6_3/mmc$ space-group symmetry. The symmetry-lowering distortions are a consequence of internal 'chemical pressure' owing to the increasing effective ionic radius of the alkaline-earth cation in the perovskite *B* site from Mg^{2+} (0.72 Å) to Ca^{2+} (1.00 Å) to Sr^{2+} (1.18 Å). Increasing the effective ionic radius further to Ba^{2+} (1.35 Å) leads to decomposition at room temperature. The driving force behind the transition from $P6_3/mmc$ to $C2/c$ is the need to alleviate underbonding of Ba^{2+} cations in the perovskite *A* site *via* octahedral rotations, while the transition from $C2/c$ to $P\bar{1}$ is driven by the need to regularize the shape of the Sb_2O_9 face-sharing octahedral dimers. *Ab initio* geometry-optimization calculations were used to find a triclinic starting model for $Ba_3SrSb_2O_9$.

1. Introduction

The hexagonal 6*H* perovskite structure most commonly forms in perovskites with very large *A*-site cations, which can be more easily accommodated in expanded 12-fold coordinate sites. They have an $(hcc)_2$-structure sequence consisting of 2/3 cubic close-packed layers and 1/3 hexagonal layers, and a general formula $A_3BM_2O_9$, where *A* is usually the large Ba^{2+} cation, *M* is usually a transition-metal cation with an open *d*-shell and an oxidation state of +4 or +5, and *B* is a cation with an oxidation state of +2 or +3. The *B* cations occupy bridging corner-sharing BO_6 octahedra and the *M* cations occupy face-sharing octahedral M_2O_9 dimers. When the *B* and *M* cations are of similar sizes the symmetry is hexagonal ($P6_3/mmc$), but when they are of significantly different sizes, tilting occurs to compensate for over-/underbonding and the symmetry is lowered (Zandbergen & Ijdo, 1983).

The 6*H* perovskites $Ba_3B^{2+}Sb^{5+}{}_2O_9$ were first reported (Blasse, 1965) for *B* = Mg, Ca, Sr, Ba, Co, Ni, Cu and Zn. The structures of $Ba_3MgSb_2O_9$ (Doi *et al.*, 2004; Istomin *et al.*, 2004), $Ba_3CoSb_2O_9$ (Doi *et al.*, 2004; Istomin *et al.*, 2004), $Ba_3NiSb_2O_9$ (Doi *et al.*, 2004; Kohl & Reinen, 1977), $Ba_3CuSb_2O_9$ (Kohl & Reinen, 1977) and $Ba_3ZnSb_2O_9$ (Lufaso *et al.*, 2005) have since been solved and refined in the ideal 6*H* perovskite ($BaTiO_3$-type) space group $P6_3/mmc$. The monoclinically distorted structure of a further phase, $Ba_3MnSb_2O_9$, has been reported in $C2/c$ (Doi *et al.*, 2004).

To the best of our knowledge there had been no further reports in the literature of $Ba_3BSb_2O_9$ for *B* = Ca, Sr or Ba until our recent solution and refinement of the high-

temperature structure of $Ba_3BaSb_2O_9$ (Ling *et al.*, 2007), which adopts the ideal $P6_3/mmc$ symmetry at 1023 K but decomposes at lower temperatures. We have now synthesized pure samples of the remaining members of this family, $Ba_3CaSb_2O_9$ and $Ba_3SrSb_2O_9$, and here we report their structures which were solved and refined in $C2/c$ and $P\bar{1}$, respectively, using a combination of synchrotron X-ray powder diffraction (S-XRD), neutron powder diffraction (NPD) and *ab initio* geometry-optimization calculations. The nature of the symmetry-lowering modes from ideal $P6_3/mmc$ symmetry are discussed in terms of the 'chemical pressure' exerted by the increasing effective ionic radius of the *B* cation from Mg → Ca → Sr → Ba.

2. Synthesis and data collection

Samples of $Ba_3BSb_2O_9$, where *B* = Ca and Sr, were synthesized by conventional solid-state reaction using reagents (of 99.98% or greater purity) purchased from commercial suppliers. The hygroscopic alkaline-earth carbonates were dried prior to use by heating at 973 K overnight. Stoichiometric mixtures of Sb_2O_5, $MgCO_3$, $BaCO_3$, and $CaCO_3$ or $SrCO_3$ were ground together in agate mortars and heated to 1073 K for 12 h, reground, and heated again to 1073 K for 12 h (all heating and cooling at 15 K min^{-1}). The samples were finally annealed at 623 K for 1 week in order to ensure that they were well crystallized in their low-temperature forms, after which they were confirmed as phase-pure on the basis of conventional (Cu $K\alpha$) X-ray diffraction (XRD) data collected on a Shimadzu XRD-6000 diffractometer.

S-XRD data for $Ba_3CaSb_2O_9$ and $Ba_3SrSb_2O_9$ were collected on the X-ray Operations and Research (XOR) beamline 1-BM-C at the Advanced Photon Source (APS), Argonne National Laboratory, using flat-plate geometry at a wavelength of 1.1823 Å. Rietveld refinements using S-XRD data were carried out using the *GSAS* suite (Larson & Von Dreele, 1994) with the EXPGUI front-end (Toby, 2001). Scale factors, zero shifts, background functions (shifted Chebyschev as implemented in *GSAS* with eight terms), peak-shape parameters (pseudo-Voigt function 'type 4', as implemented in *GSAS*, using a fixed Gaussian parameter G_P and Lorentzian parameter L_X as refined against an NBS 640c silicon standard, and refining only the strain terms S_{hkl}) and a surface roughness correction for flat-plate samples ('type 3' in *GSAS*) were refined.

NPD data for $Ba_3SrSb_2O_9$ were collected at the Institut Laue–Langevin, France, on the high-resolution diffractometer D2B. The sample was mounted in a 6 mm diameter vanadium can and data were collected at room temperature with neutrons of wavelength 1.5972 Å, with 10′ collimation and closed slits (50/50) over 5 h. The data used for the Rietveld refinements described below were integrated using only the middle 10 cm of the 30 cm detector, in order to obtain the highest possible resolution. Rietveld refinements using NPD data were carried out using *GSAS* with the EXPGUI front-end. Scale factors, zero shifts, background functions (shifted Chebyschev as implemented in *GSAS* with six terms), peak-shape parameters (pseudo-Voigt function 'type 4', as implemented in *GSAS*, refining the Gaussian parameters G_U, G_V and G_W and the Lorentzian parameter L_X).

First-principles calculations were carried out within the framework of density functional theory (DFT). We used the projector-augmented wave method (PAW; Blöchl, 1994; Kresse & Joubert, 1999), as implemented in the Vienna *ab initio* simulation package (*VASP*; Kresse & Furthmuller, 1996; Kresse & Hafner, 1993), with the Perdew–Burke–Ernzerhof (PBE; Perdew *et al.*, 1996) form of the generalized gradient approximation (GGA). Both atomic positions and unit-cell volume and shape were optimized using a plane-wave energy cut-off of 400 eV and the Brillouin zone sampling with a 4 × 4 × 2 *k* point Monkhorst–Pack (Monkhorst & Pack, 1976) mesh (16 irreducible *k* points). The symmetry-unconstrained optimization was carried out using a conjugate-gradient algorithm until the Hellmann–Feynman forces were less than 0.001 eV $Å^{-1}$ on each atom.

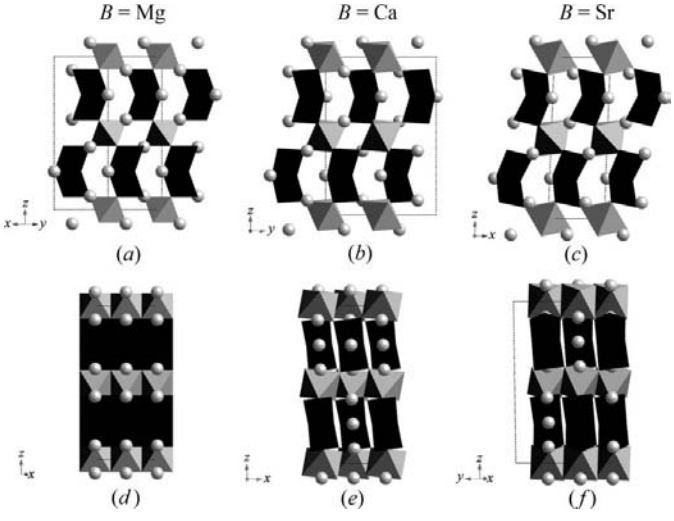

Figure 1
Polyhedral representations of the structures of $Ba_3BSb_2O_9$, *B* = Mg (Lufaso *et al.*, 2005), Ca and Sr, in equivalent projections, showing the symmetry-lowering octahedral rotations. SbO_6 octahedra are dark grey, BO_6 octahedra are light grey and Ba spheres are light grey.

3. Structure determination and refinement

Our starting point for the structure solution and refinement of $Ba_3CaSb_2O_9$ was the published room-temperature structure of $Ba_3MgSb_2O_9$ in $P6_3/mmc$ (Figs. 1*a* and 1*d*; Lufaso *et al.*, 2005). When we used this structure as a model for $Ba_3CaSb_2O_9$, peak splitting in the S-XRD data [Fig. 2 (below)] made it immediately clear that the symmetry needed to be lowered from hexagonal to monoclinic. We therefore lowered the symmetry to $C2/c$ and applied initial unit-cell distortions and atomic displacements away from the average positions based on the published structure of $Ba_3MnSb_2O_9$ (Doi *et al.*, 2004). This led to a sufficiently good fit to observed data that a Rietveld refinement could be carried out.

The unit-cell parameters and a global isotropic atomic displacement parameter (ADP) were initially refined along

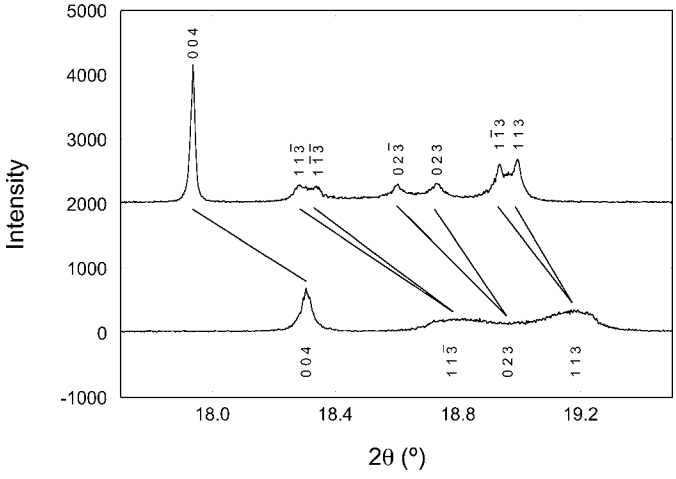

Figure 2
Part of the synchrotron XRD profiles of $Ba_3CaSb_2O_9$ (below) and $Ba_3SrSb_2O_9$ (above) at λ = 1. 1823 Å, with peaks indexed to monoclinic $C2/c$ and triclinic $C\bar{1}$ unit cells, respectively. The $C\bar{1}$ (rather than $P\bar{1}$) setting is used in order to emphasize the relationship to the $C2/c$ setting.

with the instrumental parameters described in §2 above, followed by atomic positions. The extremely large refined strain parameters (discussed in §4 below) correlated with anisotropic ADPs, and it was ultimately only possible to refine these for the two Ba atoms. 'Soft' bond-length constraints as implemented in *GSAS* were used to direct the positional refinement of the relatively light O atoms towards regular bond lengths for Ba—O [3.05 (5) Å], Ca—O [2.31 (3) Å] and Sb—O [1.97 (3) Å], and regular octahedra for CaO_6 [O—O bond lengths 3.25 (5)/3.27 (5) Å] and SbO_6 [O—O bond lengths 2.78 (5) Å]. It was necessary to constrain the isotropic ADPs of the O atoms that form the common octahedral face of the Sb_2O_9 dimers (O1 and O2) to be equivalent. Finally, a small number of weak remaining peaks were accounted for by the incorporation of two impurity phases, neither of which had been evident in previously collected laboratory XRD data: CaO [0.45 (6) wt %] and an $Fm3m$ [a = 8.44568 (17) Å] perovskite similar to Ba_2YNbO_6, modelled as Ba_2CaSbO_6 [11.3 (2) wt %].

Full experimental details and final refinement statistics for $Ba_3CaSb_2O_9$ are presented in Table 1,[1] with the final Rietveld fit shown in Fig. 3. The final refined structure parameters and empirical bond-valence sums (BVS; Brese & O'Keeffe, 1991) are presented in Table 2. The structure is shown in polyhedral representation in Figs. 1(*b*) and 1(*e*).

The refined structure of $Ba_3CaSb_2O_9$ was then used as the starting point for our model of $Ba_3SrSb_2O_9$. Comparison of this model with S-XRD data revealed peak splitting clearly indicative of a symmetry-lowering from monoclinic to triclinic [Fig. 2 (top)]. In order to develop a triclinic model for $Ba_3SrSb_2O_9$, we carried out a symmetry-unconstrained *ab inito* DFT geometry optimization on the monoclinic $C2/c$ starting model (the details of which are described in §2). The optimized model was found to possess triclinic (but centrosymmetric) $P\bar{1}$ symmetry to within 0.01 Å on all sites, but to have deviated from $C2/c$ symmetry by more than 0.2 Å. This optimized model provided a satisfactory fit to the S-XRD data. However, although this model could be refined to provide a good fit to the S-XRD data, the refined model has unsatisfactorily large standard deviations associated with O-

Table 1
Experimental details.

	$Ba_3CaSb_2O_9$	$Ba_3SrSb_2O_9$
Crystal data		
Chemical formula	$Ba_3CaSb_2O_9$	$Ba_3SrSb_2O_9$
M_r	839.56	887.10
Cell setting, space group	Monoclinic, $C2/c$	Triclinic, $P\bar{1}$
Temperature (K)	298	298
a, b, c (Å)	5.99898 (7), 10.37797 (19), 14.8658 (3)	6.08467 (15), 6.08608 (15), 15.1934 (3)
α, β, γ (°)	90, 91.384 (2), 90	89.175 (2), 88.485 (2), 119.7431 (11)
V (Å^3)	925.23 (3)	488.10 (2)
Z	4	2
D_x (Mg m^{-3})	6.0253 (2)	6.0341 (2)
Radiation	Synchrotron, λ = 1.182279 Å	Neutron, λ = 1.597248 Å
μ (mm^{-1})	18.976	0.00233
Specimen form, colour	Flat plate, white	Cylinder, white
Specimen size (mm)	10 × 10	20 × 6
Specimen preparation cooling rate (K min^{-1})	15	15
Specimen preparation pressure (kPa)	101	101
Specimen preparation temperature (K)	1073	1073
Data collection		
Diffractometer	Point detector	64 × ^{3}He tubes
Data collection method	Specimen mounting: flat plate; mode: reflection; scan method: step	Specimen mounting: vanadium can; mode: transmission; scan method: step
Aborption correction	Surface roughness (*GSAS* type 2)	Cylinder (Lobanov & Alte da Veiga, 1998)
T_{min}	–	0.081
T_{max}	–	0.190
2θ (°)	$2\theta_{min}$ = 4.999934, $2\theta_{max}$ = 64.99993, increment = 0.003	$2\theta_{min}$ = 0.1498, $2\theta_{max}$ = 158.7998, increment = 0.05
Refinement		
Refinement method	Rietveld	Rietveld
R factors and goodness-of-fit	R_p = 0.156, R_{wp} = 0.204, R_{exp} = 0.104, S = 1.96	R_p = 0.051, R_{wp} = 0.067, R_{exp} = 0.167, S = 0.40
Wavelength of incident radiation (Å)	1.1823	1.5972
Excluded region(s)	none	none
Profile function	Pseudo-Voigt	Pseudo-Voigt
χ^2	2.017	0.1634†
No. of reflections	434	1938
No. of parameters	49	76
$(\Delta/\sigma)_{max}$	0.05	0.04

Computer programs used: *GSAS* (Larson & Von Dreele, 1994). † Note that because of technical difficulties it was not possible to subtract an experimental background from these data, leading to the overestimation of $\sigma(I) = I^{1/2}$ for each data point and hence an overestimation of R_{exp}, and ultimately to $\chi^2 = [wR_p/R_{exp}]^2 < 1$. An alternative estimate of the goodness-of-fit could be obtained by performing a Le Bail refinement, using the same free variables as the Rietveld refinement and calculating $[wR_p(\text{Rietveld})/wR_p(\text{Le Bail})]^2 = [0.0665/0.0523]^2 = 1.617$.

[1] Supplementary data for this paper are available from the IUCr electronic archives (Reference: KD5019). Services for accessing these data are described at the back of the journal.

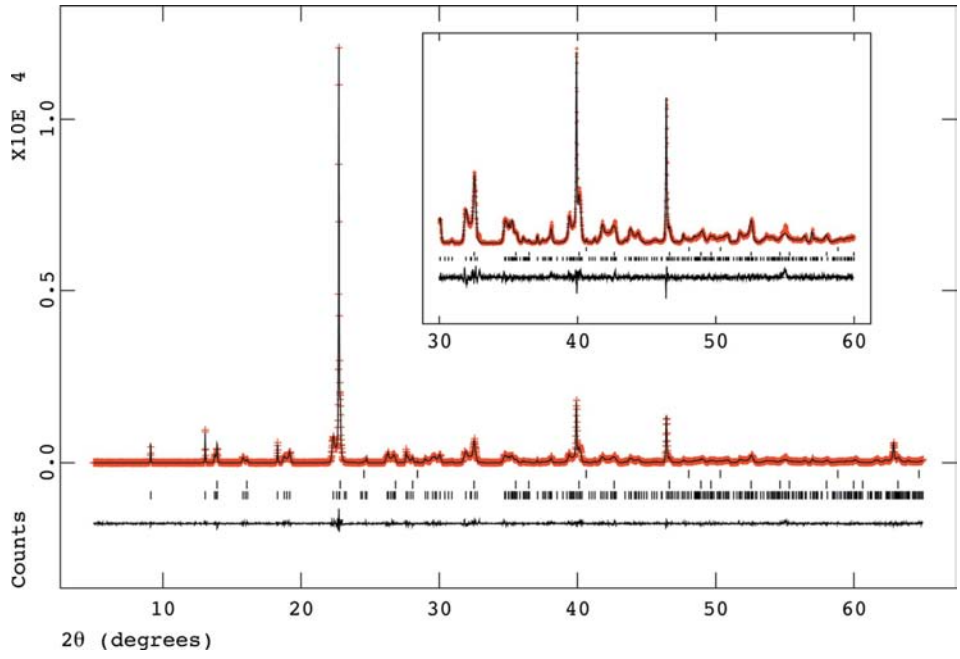

Figure 3
Observed (crosses), calculated (solid line) and difference (below) synchrotron XRD profiles of $Ba_3CaSb_2O_9$ at λ = 1.1823 Å. The reflection markers refer to $Ba_3CaSb_2O_9$ (bottom), the Ba_2YNbO_6-type impurity (middle) and the CaO impurity (top).

Table 2
Refined structural parameters and empirical bond-valence sums (BVS; Brese & O'Keeffe, 1991) for $Ba_3CaSb_2O_9$ at 298 K.

Superscript numbers indicate constraints.

	x	*y*	*z*	$100U_{iso}$	BVS
Ba1	0	−0.0031 (3)	1/4	1.67†	1.77 (14)
Ba2	0.0096 (2)	0.3325 (3)	0.09298 (7)	1.68†	1.595 (13)
Ca1	0	0	0	1.02 (18)	2.67 (3)
Sb1	−0.0176 (2)	0.3339 (3)	0.84544 (6)	1.63 (8)	5.35 (6)
O1	0	0.5149 (11)	1/4	1.2 (3)[1]	1.80 (2)
O2	0.2818 (14)	0.2387 (8)	0.2417 (4)	1.2 (3)[1]	1.95 (3)
O3	0.0244 (15)	0.8247 (7)	0.0883 (5)	3.2 (6)	2.07 (3)
O4	0.2931 (12)	0.0816 (9)	0.0834 (5)	4.0 (5)	2.03 (3)
O5	0.7521 (13)	0.0817 (9)	0.0973 (5)	4.4 (6)	2.2 (4)

† Equivalent isotropic *U* for atoms refined with anisotropic ADPs.

atom positions and ADPs owing to the large number of independent O-atom positions and the relatively low sensitivity of X-rays to them in the presence of heavy elements such as Sb and Ba. NPD data were therefore used for the Rietveld refinement of this model.

The unit-cell parameters and a global isotropic ADP were initially refined along with the instrumental parameters described in §2 above, followed by atomic positions. Refinement of independent ADPs for each site led to slightly negative ADPs for some of the metal-atom sites, which were corrected by applying the empirical absorption correction for cylindrical samples of Lobanov & Alte da Veiga (1998), as implemented in *GSAS*. The introduction of anisotropic ADPs led to only a small improvement in the refinement statistics, but to non-positive definite ADPs for the Ba3 site; therefore, the final refinement was carried out with isotropic ADPs.

Full experimental details and final refinement statistics for $Ba_3SrSb_2O_9$ are presented in Table 1, with the final Rietveld fit shown in Fig. 4. The final refined structure parameters, shifts relative to the DFT-optimized positions and empirical BVS are presented in Table 3. The structure is shown as a polyhedral representation in Figs. 1(*c*) and 1(*f*).

4. Discussion

The 'chemical pressure' effects produced by changing the size of the *B* cation in $Ba_3BSb_2O_9$, and the resolution of that pressure through symmetry-lowering octahedral rotations, can clearly be seen in Fig. 1.

For *B* = Mg, the MgO_6 octahedra are only slightly larger than the SbO_6 octahedra, allowing them to fit together in $P6_3/mmc$ symmetry with no octahedral rotations. This is in line with the effective ionic radii (IR; Shannon, 1976) of Mg^{2+} (0.720 Å) and Sb^{5+} (0.60 Å) in sixfold coordination.

For *B* = Ca, the CaO_6 octahedra are significantly larger [IR(Ca^{2+}) = 1.00 Å in sixfold coordination] than the SbO_6 octahedra. This misfit is accommodated by symmetry-lowering rotations of the octahedral units about the *c* and *b* axes. However, it is clear from Fig. 2 that the structure still contains highly anisotropic strain. From the Rietveld refinement (Fig. 3), this strain was found to be strongest in the ⟨011⟩ direction, along which direction it can be seen by comparison of Figs. 1(*e*) and 1(*d*) that the CaO_6 octahedra are significantly distorted from their ideal form.

For *B* = Sr, where the SrO_6 octahedra are even larger [IR(Sr^{2+}) = 1.18 Å in sixfold coordination] compared with the SbO_6 octahedra, this strain is relieved by a further symmetry-lowering transition to $P\bar{1}$. The key distortion driving this transition is the rotation of Sb_2O_9 face-sharing octahedral dimers about the *a* axis of the monoclinic cell, as can be seen by comparing Figs. 1(*d*) and 1(*e*) – note that the mirror plane through the dimers perpendicular to *c* that is enforced in *C*2/*c* symmetry is removed in $P\bar{1}$, relieving the distortion of the SrO_6 octahedra.

In the most extreme case of *B* = Ba [IR(Ba^{2+}) = 1.35 Å in sixfold coordination], for which we recently published the high-temperature (1023 K) structure in $P6_3/mmc$ (Ling *et al.*, 2007), we could not obtain a single-phase $P\bar{1}$ sample at room temperature. In fact, all attempts to anneal the sample at low

temperatures as for B = Ca and Sr led to a multi-phase mixture, including at least one identifiable impurity, $BaSb_2O_6$ (DeBoer *et al.*, 1994; see Fig. 1 of Ling *et al.*, 2007). It appears that the size mismatch between $Ba^{2+}O_6$ and $Sb^{5+}O_6$ octahedra in a 6*H* perovskite topology is simply too great to be resolved at room temperature, even by lowering the symmetry to monoclinic or triclinic.

Finally, it is worth reiterating the extremely useful role that DFT geometry-optimization calculations played in the determination of the structure of $Ba_3SrSb_2O_9$. Although the triclinic unit cell could be unambigiously indexed from S-XRD data, it would have been extremely difficult to test all the possible symmetry-lowering modes from the monoclinic model and compare the results of refining them against high-resolution NPD data. Furthermore, there would always have been some doubt as to the uniqueness of the final refined solution thus obtained. The extremely small differences (< 0.15 Å, see Table 3) between the DFT-optimized and Rietveld-refined models, and the excellent quality of that refinement, greatly increase our confidence in the result. It is also interesting that *ab initio* DFT methods can successfully model these structures, despite the relatively poor results of empirical BVS calculations. Tables 2 and 3 show that, while the BVS of all O^{2-} anions are reasonable for $Ba_3CaSb_2O_9$ in $C2/c$ and $Ba_3SrSb_2O_9$ in $P\bar{1}$, in both cases the Ba^{2+} cations in the perovskite A sites are quite underbonded and the Ca/Sr^{2+} cations in the perovskite B sites are seriously overbonded. In other words, the symmetry-lowering transition cannot be easily explained in terms of octahedral rotations that improve the BVS of the cations. The only BVS results that shed any light on this are for the Sb^{5+} cations, which improve slightly from 5.35 (6) in monoclinic $Ba_3CaSb_2O_9$ to 5.17 (15) and 5.26 (15) in triclinic $Ba_3SrSb_2O_9$, supporting the observation from Fig. 1 that the symmetry-lowering allows the Sb_2O_9 face-sharing octahedral dimers to become more regular in shape by rotating about the a axis of the monoclinic cell.

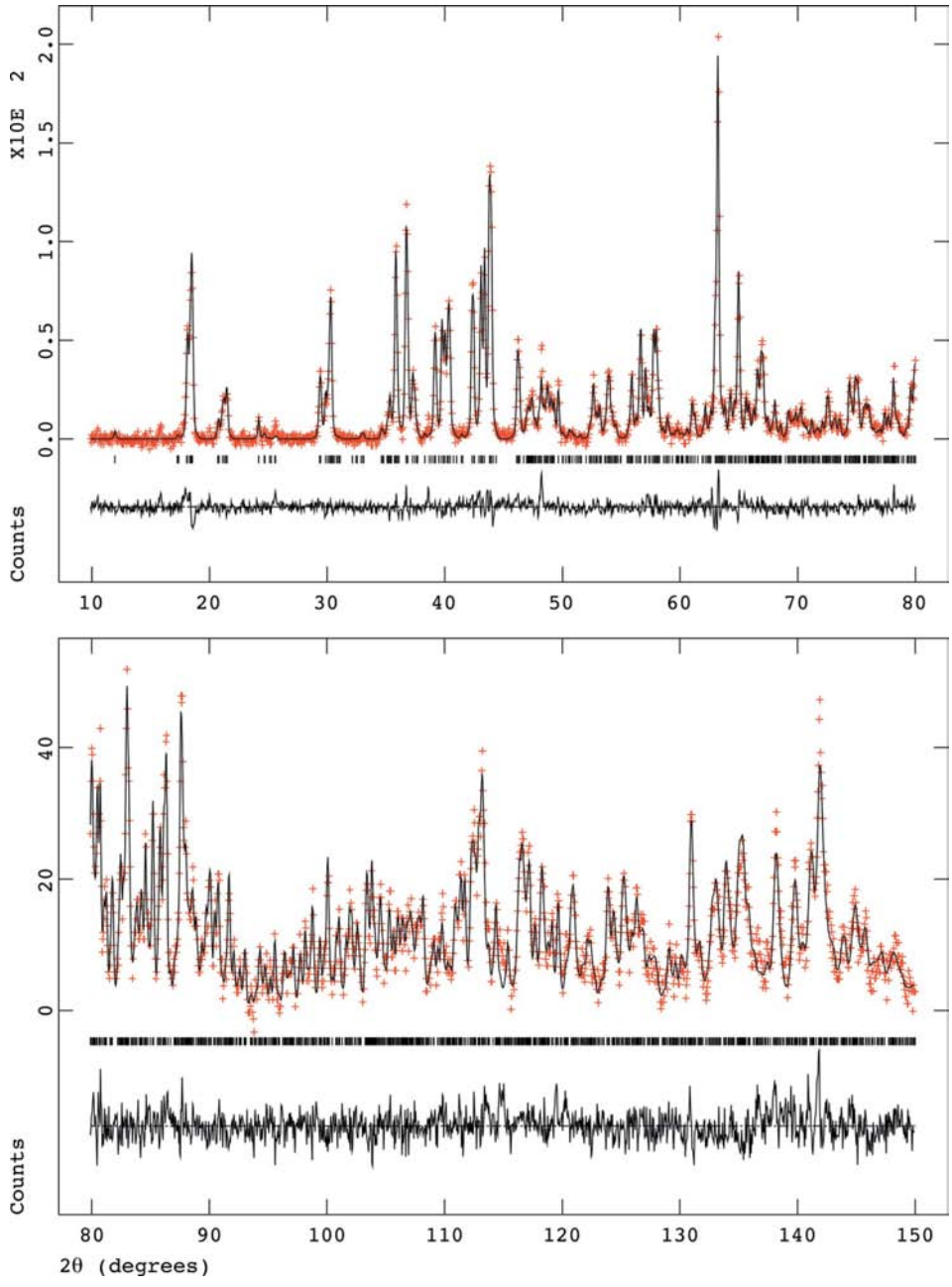

Figure 4
Observed (crosses), calculated (solid line) and difference (below) NPD profiles of $Ba_3SrSb_2O_9$ at λ = 1.5972 Å.

5. Conclusion

The compounds $Ba_3CaSb_2O_9$ and $Ba_3SrSb_2O_9$ have 6*H* hexagonal perovskite structures closely related to that of $Ba_3MgSb_2O_9$. However, while $Ba_3MgSb_2O_9$ has the ideal hexagonal $P6_3/mmc$ symmetry, $Ba_3CaSb_2O_9$ is monoclinic $C2/c$ and $Ba_3SrSb_2O_9$ is triclinic $P\bar{1}$. The symmetry-lowering distortions are a consequence of internal 'chemical pressure' owing to the increasing effective ionic radius of the alkaline-earth cation in the perovskite B site from Mg^{2+} (0.72 Å) to Ca^{2+} (1.00 Å) to Sr^{2+} (1.18 Å). Increasing the effective ionic radius further to Ba^{2+}

Table 3
Refined structural parameters, empirical bond-valence sums (BVS; Brese & O'Keeffe, 1991) and shifts relative to the DFT-optimized positions for $Ba_3SrSb_2O_9$ at 298 K.

	x	*y*	*z*	$100U_{iso}$	BVS	Shift (Å)
Ba1	0.9851 (17)	0.0034 (18)	0.7502 (7)	2.67 (14)	1.845 (17)	0.035
Ba2	0.3469 (15)	0.6798 (17)	0.9008 (6)	2.68 (17)	1.511 (14)	0.049
Ba3	0.3194 (15)	0.6562 (14)	0.5962 (5)	2.04 (14)	1.527 (15	0.043
Sb1	0.3089 (13)	0.6474 (14)	0.1562 (5)	1.86 (11)	5.17 (15)	0.031
Sb2	0.3616 (14)	0.6910 (14)	0.3422 (5)	1.76 (11)	5.26 (15)	0.045
Sr1	0	0	0	2.19 (15)	2.81 (5)	0
Sr2	0	0	1/2	1.31 (12)	2.82 (5)	0
O1	0.5313 (13)	0.4866 (13)	0.7518 (6)	2.86 (14)	1.84 (7)	0.065
O2	0.5176 (14)	0.0477 (13)	0.7644 (5)	2.58 (14)	1.97 (7)	0.069
O3	0.8774 (14)	0.2159 (15)	0.8982 (5)	3.21 (17)	2.16 (8)	0.144
O4	0.4256 (13)	0.2380 (14)	0.9308 (5)	2.83 (16)	1.98 (8)	0.093
O5	0.8926 (14)	0.6939 (14)	0.8898 (6)	2.93 (15)	2.09 (7)	0.123
O6	0.9526 (12)	0.4688 (13)	0.7325 (5)	2.21 (13)	1.91 (7)	0.050
O7	0.7512 (13)	0.1069 (14)	0.5942 (5)	2.61 (15)	2.081 (7)	0.132
O8	0.7823 (15)	0.5850 (14)	0.5730 (6)	3.22 (17)	1.92 (8)	0.109
O9	0.3062 (13)	0.1462 (14)	0.6116 (5)	2.67 (15)	2.17 (8)	0.113

(1.35 Å) leads to decomposition at room temperature. The driving force behind the transition from $P6_3/mmc$ to $C2/c$ appears to be the need to alleviate underbonding of Ba^{2+} cations in the perovskite *A* site *via* octahedral rotations, while the transition from $C2/c$ to $P\bar{1}$ appears to be driven by the need to regularize the shape of the Sb_2O_9 face-sharing octahedral dimers. *Ab initio* (DFT) geometry-optimization calculations were found to be a useful adjunct to Rietveld refinement of neutron powder diffraction data in the case of $Ba_3SrSb_2O_9$, both for finding a triclinic starting model and for verifying the result.

Synchrotron XRD data were collected with the financial support of the Australian Synchrotron Research Program (ASRP), and neutron powder diffraction data were collected with the financial support of the Access to Major Research Facilities Program (AMRFP). Use of the Advanced Photon Source was supported by the US Department of Energy, Office of Science, Office of Basic Energy Sciences, under Contract No. DE-AC02-06CH11357. The authors would like to thank Dr J. A. Kaduk for useful discussions regarding the refinement of the synchrotron XRD data.

References

Blasse, G. (1965). *J. Inorg. Nucl. Chem.* **27**, 993–1003.
Blöchl, P. E. (1994). *Phys. Rev. A*, **50**, 17953–17979.
Brese, N. E. & O'Keeffe, M. (1991). *Acta Cryst.* B**47**, 192–197.
DeBoer, B. G., Young, R. A. & Sakthivel, A. (1994). *Acta Cryst.* C**50**, 476–482.
Doi, Y. S., Hinatsu, Y. & Ohoyama, K. (2004). *J. Phys. Condens. Matter*, **16**, 8923–8935.
Istomin, S. Y., Koutcenko, V. A., Antipov, E. V., Lindberg, F. & Svensson, G. (2004). *Mater. Res. Bull.* **39**, 1013–1022.
Kohl, P. & Reinen, D. (1977). *Z. Anorg. Allg. Chem.* **433**, 81–93.
Kresse, G. & Furthmuller, J. (1996). *Phys. Rev. B*, **54**, 11169–11186.
Kresse, G. & Hafner, J. (1993). *Phys. Rev. B*, **47**, 558–561.
Kresse, G. & Joubert, D. (1999). *Phys. Rev. B*, **59**, 1758–1775.
Larson, A. C. & Von Dreele, R. B. (1994). *GSAS*, Report LAUR 86–748. Los Alamos National Laboratory, New Mexico, USA.
Ling, C. D., Avdeev, M. & Aivazian, K. (2007). *Acta Cryst.* B**63**, 584–588.
Lobanov, N. N. & Alte da Veiga, L. (1998). *Proceedings of the 6th European Conference on Powder Diffraction (EPDIC 6)*, Budapest, Hungary, 22–25 August, pp. 12–16. Zurich: Trans Tech Publications.
Lufaso, M. W., Hopkins, E., Bell, S. M. & Llobet, A. (2005). *Chem. Mater.* **17**, 4250–4255.
Monkhorst, H. J. & Pack, J. D. (1976). *Phys. Rev. B*, **13**, 5188–5192.
Perdew, J. P., Burke, K. & Ernzerhof, M. (1996). *Phys. Rev. Lett.* **77**, 3865–3868.
Shannon, R. D. (1976). *Acta Cryst.* A**32**, 751–767.
Toby, B. H. (2001). *J. Appl. Cryst.* **34**, 210–213.
Zandbergen, H. W. & IJdo, D. J. W. (1983). *Acta Cryst.* C**39**, 829–832.